



OPEN

Heating-mediated purification of active FGF21 and structure-based design of its variant with enhanced potency

Ye-Eun Jung^{1,7}, Kyeong Won Lee^{2,7}, Jae Hyun Cho^{3,7}, Da-Woon Bae¹, Bo-Gyeong Jeong¹, Yeon-Ju Jung¹, Soo-Bong Park¹, Young Jun An², Kyungchan Kim³, Ga Seul Lee⁴, Lin-Woo Kang⁵, Jeong Hee Moon⁴, Jung-Hyun Lee², Eun-Kyoung Kim^{3,6}, Hyung-Soon Yim² & Sun-Shin Cha¹

Fibroblast growth factor 21 (FGF21) has pharmaceutical potential against obesity-related metabolic disorders, including non-alcoholic fatty liver disease. Since thermal stability is a desirable factor for therapeutic proteins, we investigated the thermal behavior of human FGF21. FGF21 remained soluble after heating; thus, we examined its temperature-induced structural changes using circular dichroism (CD). FGF21 showed inter-convertible temperature-specific CD spectra. The CD spectrum at 100 °C returned to that at 20 °C when the heated FGF21 solution was cooled. Through loop swapping, the connecting loop between β 10 and β 12 in FGF21 was revealed to be associated with the unique thermal behavior of FGF21. According to surface plasmon resonance (SPR) experiments, *in vitro* cell-based assays, and model high-fat diet (HFD)-induced obesity studies, heated FGF21 maintained biological activities that were comparable to those of non-heated and commercial FGF21s. Based on sequence comparison and structural analysis, five point-mutations were introduced into FGF21. Compared with the wild type, the heated FGF21 variant displayed improved therapeutic potential in terms of body weight loss, the levels of hepatic triglycerides and lipids, and the degree of vacuolization of liver in HFD-fed mice.

Fibroblast growth factors (FGFs) regulate various developmental and metabolic processes, including cell proliferation, differentiation, angiogenesis, wound healing, nerve regeneration, chronic inflammation, and cancer growth^{1,2}. The FGF family consists of 22 members that share the β -trefoil fold despite their relatively low sequence identities (13–71%)³. The β -trefoil fold contains 12 β -strands that form 6 two-stranded β -hairpins (i.e., β 1– β 12, β 2– β 3, β 4– β 5, β 6– β 7, β 8– β 9, and β 10– β 11). Hairpins are arranged in a pseudo three-fold symmetry: the first, third, and fifth β -hairpins form a barrel that is covered by a triangular cap consisting of the second, fourth, and sixth β -hairpins^{3,4}.

FGFs are divided into FGF1, FGF4, FGF7, FGF8, FGF9, FGF11, and FGF19 subfamilies depending on their sequence similarities. Except for the intracellular FGF11 subfamily, FGFs form complexes with FGF receptors (FGFRs) on the cell membrane, which are generally composed of three immunoglobulin (Ig)-like extracellular domains, a transmembrane domain, and a cytoplasmic tyrosine kinase domain^{2,3,5}. FGFs bind to the interface between the second and third Ig-like ectodomains to induce receptor dimerization, leading to the phosphorylation of tyrosine residues in the cytoplasmic domain to stimulate signaling pathways^{1,2,6}.

The canonical FGFs (FGF1, FGF4, FGF7, FGF8, and FGF9 subfamilies) have a positively charged sector clustered by lysine and arginine residues and thus display avidity for negatively charged heparin/heparan sulfate

¹Department of Chemistry & Nanoscience, Ewha Womans University, Seoul 03760, Republic of Korea. ²Marine Biotechnology Research Center, Korea Institute of Ocean Science and Technology, 385 Haeyang-Ro, Busan 49111, Republic of Korea. ³Department of Brain Sciences, Daegu Gyeongbuk Institute of Science and Technology, Daegu 42988, Republic of Korea. ⁴Disease Target Structure Research Center, Korea Research Institute Bioscience and Biotechnology (KRIBB), Daejeon 34141, Republic of Korea. ⁵Department of Biological Sciences, Konkuk University, Seoul 05029, Republic of Korea. ⁶Neurometabolomics Research Center, Daegu Gyeongbuk Institute of Science and Technology, Daegu 42988, Republic of Korea. ⁷These authors contributed equally: Ye-Eun Jung, Kyeong Won Lee and Jae Hyun Cho. ✉email: ekkim@dgist.ac.kr; yimh@kiost.ac.kr; chajung@ewha.ac.kr

proteoglycans (HSPGs) present on the cell surface or in the extracellular matrix⁷. Therefore, canonical FGFs form ternary complexes with HSPG and FGFR, and act in the vicinity of cells as paracrine and/or autocrine factors. Conversely, FGF19 subfamily members (FGF19, FGF21, and FGF23) have no apparent HSPG-binding site on their surfaces and thus perform their physiological roles in an endocrine manner⁸. They are released from the extracellular matrix and reach remote target organs through the bloodstream⁹.

A remarkable structural feature of FGF19 subfamily members, including FGF21, is the presence of an additional C-terminal loop protruding from the β -trefoil core structure. The long C-terminal loop comprising ~30 residues tightly binds to α -Klotho¹⁰ or β -Klotho^{11,12}, known as the co-receptors of FGF23 or FGF19 and FGF21, respectively. The truncation of the C-terminal tail or the absence of Klotho causes severe defects in FGF signaling, demonstrating the critical role of the interaction between the C-terminal loop and Klotho^{10,13,14}.

Since Klothos are membrane-bound proteins expressed in certain organs, their presence determines the tissue selectivity of FGF19 subfamily members that form the ternary FGF-FGFR-Klotho complex^{15,16}. β -Klotho is mainly distributed in adipose tissues, the liver, and the pancreas, indicating that those are the target sites of FGF21^{17–19}; in fact, FGF21 has been implicated in glucose and lipid metabolism^{16,20,21}. Administration of FGF21 to rodents or non-human primates causes a reduction in fat mass and body weight, as well as levels of circulating glucose and triglycerides (TG), and improves insulin sensitivity and energy metabolism^{21–23}. Therefore, FGF21 shows therapeutic potential to treat obesity-related metabolic complications, including hyperglycemia, insulin resistance, and non-alcoholic fatty liver disease (NAFLD)^{24–27}.

There are several hurdles that should be tackled to develop FGF21 for clinical application. For example, the C-terminal loop of FGF21 is essential for its activity due to strong interactions with β -Klotho, but it is highly susceptible to proteolytic attack^{28–31}. Proteases in expression hosts can inactivate FGF21 by breaking this loop during purification processes. Heating that precipitates heat-labile host proteases can minimize the proteolytic degradation of the C-terminal loop, if FGF21 endures heat treatment. In this study, we discovered the unreported thermal behavior of human FGF21 and employed this property for efficient purification of active human FGF21 (hereafter, FGF21). Additionally, structure-based designing was performed to develop FGF21 variants with point-mutations in the C-terminal region interacting with β -Klotho, which displayed enhanced potency for *in vitro* and *in vivo* studies compared with the wild type.

Results

Temperature-responsive structural reversibility of FGF21. To investigate how susceptible FGF21 is to thermal denaturation, FGF21-containing solutions were incubated at high temperatures for 10 min. When proteins are denatured, they form coarse aggregate particles that scatter visible light to make solutions turbid. There was no change in turbidity of FGF21 solutions stored at 20 °C after incubation at 40, 60, 80, and 100 °C, when observed by naked eyes, indicating the absence of large protein aggregates (Supplementary Fig. S1). In contrast, FGF2 solutions irreversibly became turbid after heating; turbidity was maintained regardless of storing temperatures (Supplementary Fig. S1). To confirm that FGF21 is resistant to thermal denaturation, the heat-treated FGF21 solutions were centrifuged to remove protein aggregates, and then supernatants were analyzed using SDS-PAGE. As shown in Fig. 1A, the amount of FGF21 in the solutions remained at almost 30 mg/mL before and after heat treatment, indicating that no protein aggregates were formed due to thermal denaturation. However, FGF2 was dramatically reduced in supernatants after incubation at 40 °C or more (Fig. 1A).

Thermal denaturation curve is a good indicator for assessing the thermal stability of proteins. To assess the thermal denaturation of FGF21 using CD spectroscopy, spectral changes were monitored at 215 nm at a temperature range of 20–100 °C^{32,33}. The FGF21 spectra displayed gradual changes as a function of temperature, which contrasted with the steep transition slope of the FGF2 spectra (Fig. 1B,C). The magnitude of enthalpy and entropy changes was smaller in FGF21 than FGF2 (Fig. 1B,C), and the T_m values were estimated to be 62.26 ± 0.6306 °C and 52.69 ± 0.1991 °C for FGF21 and FGF2, respectively.

For further characterization of the temperature responsiveness of FGF21, we examined the secondary and tertiary structural states of FGF21 as the temperature increased from 20 to 100 °C by measuring far-UV (190–260 nm) and near-UV (240–340 nm) CD spectra, respectively³⁴. In both CD spectra, temperature-induced spectral changes are sequential; for example, the spectrum at 60 °C is located between those at 40 °C and 80 °C (Fig. 2A,B). The spectral feature of FGF21 accompanied by temperature change encouraged us to measure the CD spectra while cooling the heated FGF21 solutions. The CD spectra of FGF21 at 20 °C were virtually identical to that of FGF21 that was cooled to 20 °C after heating at 100 °C (Fig. 2C,D), indicating that structural changes of FGF21 induced by heating can be restored by cooling (Fig. 2E). Consequently, FGF21 is highly likely to have temperature-responsive structural reversibility.

The unique loop region associated with the heat response of FGF21. The N- and C-terminal loops extending out from the β -trefoil core structure of FGF21 (core-FGF21) show large sequential disparities when compared with the corresponding regions of other FGFs (Supplementary Fig. S2). Therefore, we constructed a deletion mutant without the N-terminal loop ($\Delta 29$ –40) and C-terminal loop ($\Delta 174$ –209) to investigate whether both distinct terminal loops are related to the remarkable response of FGF21 to heating. However, similar to the wild type FGF21, the deletion mutant remained soluble at a concentration of ~30 mg/mL after high-temperature incubations (Fig. 1A), indicating that core-FGF21 is responsible for the thermal behavior of FGF21.

FGFs share the β -trefoil core structure with disparities in loop regions connecting β -strands^{3,4}. Among connecting loops, the $\beta 10$ – $\beta 12$ loop (residues His145–Pro161) of FGF21 is outstanding in that it has a unique amino acid composition. First, the sequence identities of the $\beta 10$ – $\beta 12$ loop in FGF21 to corresponding loops in other FGFs lie in the range of 5–25%, whereas the entire FGF21 shows 14–36% sequence identities to other FGFs. Second, the $\beta 10$ – $\beta 12$ loop of FGF21 contains 5 proline residues, constituting 29.4% of the loop, which contrasts

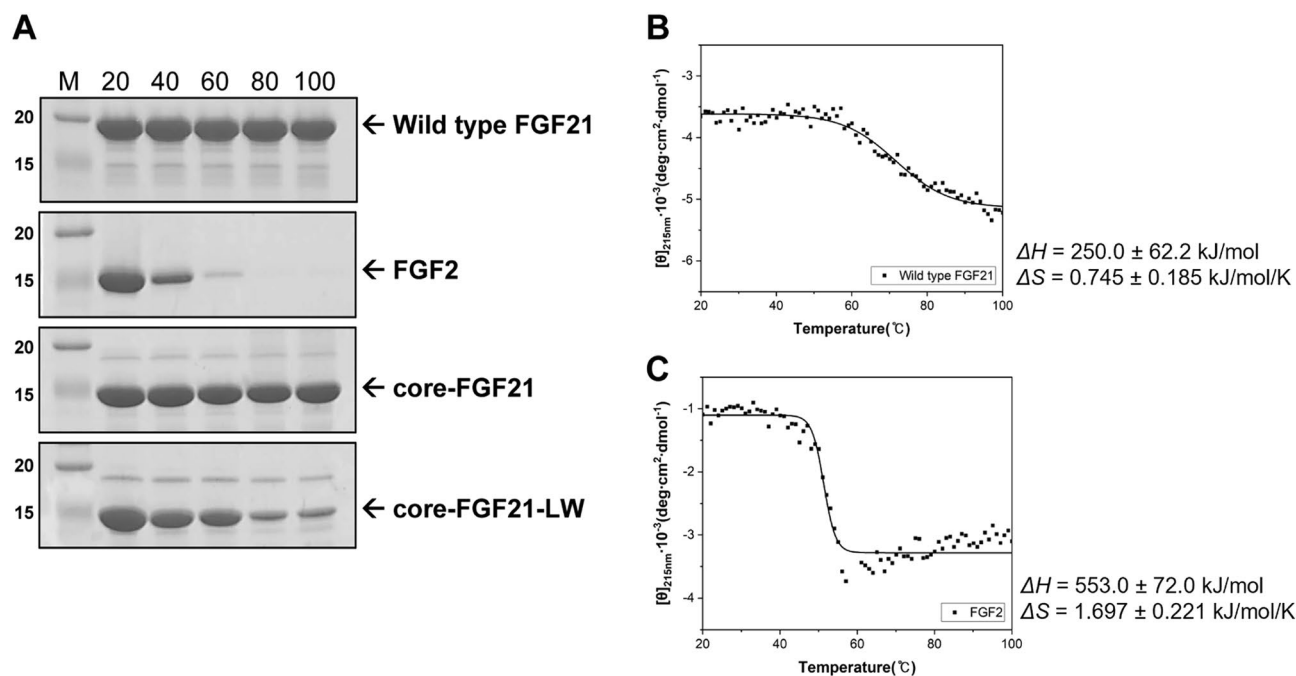


Figure 1. Monitoring the thermal denaturation of FGF21. (A) SDS-PAGE. M represents protein markers whose sizes are given in kDa on the left. Numbers in the top are incubation temperatures (°C). Arrows point out the position of target proteins. The original gels are presented in Supplementary Fig. S14. Thermal denaturation curves of FGF21 (B) and FGF2 (C). Spectral curves were fitted using the molar ellipticity $[\theta]$ values shown as dots.

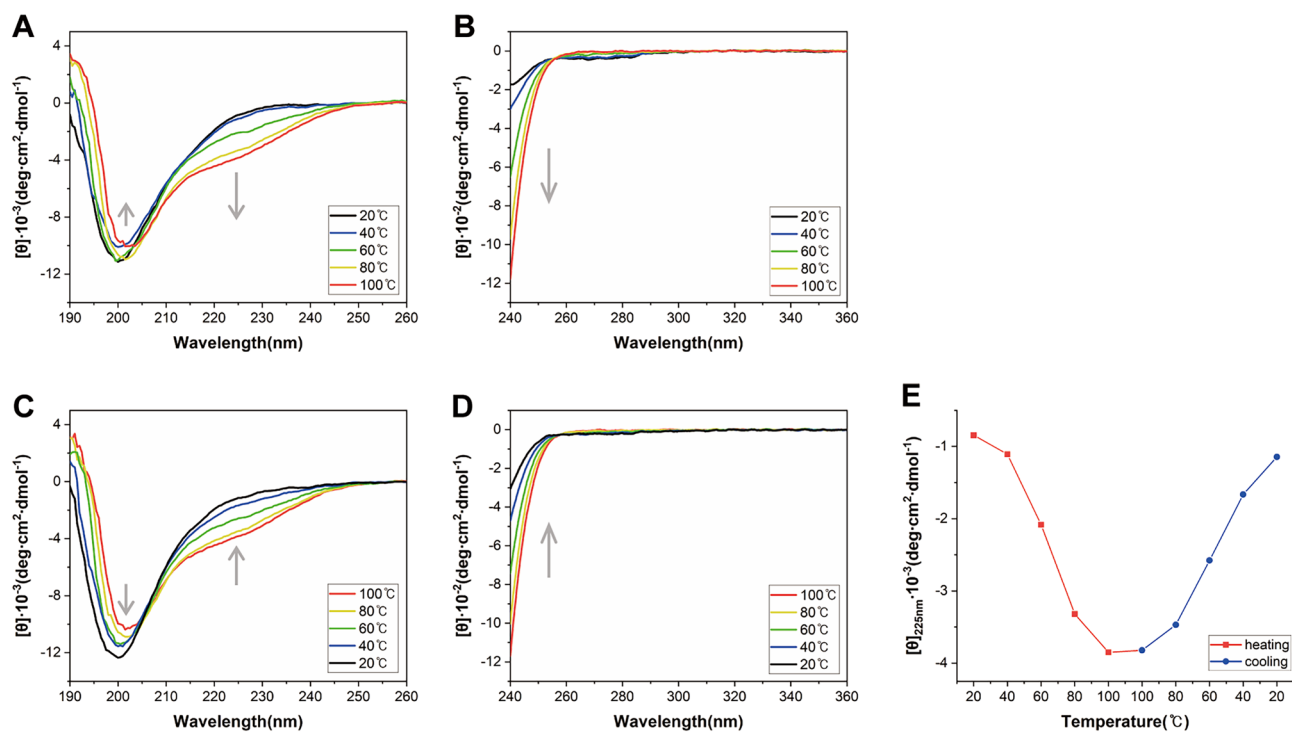


Figure 2. Temperature-dependent CD spectra of the wild type FGF21. Far-UV CD spectra upon heating (A) and cooling (C), and near-UV CD spectra upon heating (B) and cooling (D). Profiles at different temperatures are represented using different colored lines as shown in the right box of the figure. Gray arrows indicate the directions of spectral changes during heating and cooling. (E) The molar ellipticity $[\theta]$ values as temperature increases and decreases are colored in red and blue, respectively. For this figure, $[\theta]$ of FGF21 at 225 nm was used since far-UV CD spectral changes were dramatic at this wavelength.

with the fact that most FGFs have 0 or 1 proline residue in the corresponding loop (Supplementary Fig. S2). Proline residues in loop regions have been reported to contribute to the thermal stability of proteins^{35,36}.

Based on these analyses, we tested the contribution of the unique β 10– β 12 loop to the thermal response of FGF21 through loop swapping. Sequence identities among the β 10– β 12 loops of FGFs were low (Supplementary Fig. S2), which led us to hypothesize that rather than individual residues, the overall feature of the β 10– β 12 loop is associated with the unique thermal behavior of FGF21. This was the reason why we took the loop swapping strategy instead of point mutations. Our aim was to design a mutant that is sensitive to heat treatment but maintains structural and functional properties of the wild type FGF21. When the β 10– β 12 loop of FGF21 was replaced by the corresponding region of FGF2, we failed to get soluble form of the mutant, which indicates defects in folding or structural integrity. As an alternative, we searched for another FGF protein with the β 10– β 12 loop that is similar to that of FGF21. The β 10– β 12 loop of FGF23 shows a relatively high sequence identity to that of FGF21 and furthermore, the FGF23 loop adopts a random coil conformation like the β 10– β 12 loop of FGF21 (Supplementary Fig. S2). In terms of overall feature, the β 10– β 12 loop of FGF23 seemed to be suitable for loop swapping with minimal structural and functional effect (Fig. 3). Therefore, the β 10– β 12 loop of core-FGF21 was replaced by the corresponding loop (residues 137–154) of FGF23 to make a loop-swapped mutant (core-FGF21-LW).

As shown in Fig. 1A, the amount of core-FGF21 in solutions was nearly identical, regardless of heat treatment. However, core-FGF21-LW in supernatants was reduced by more than 85% after 10 min incubations at 80 °C and 100 °C (Fig. 1A, Supplementary Fig. S1). The formation of protein aggregates was monitored by measuring optical density since aggregates scatter visible light strongly due to their large sizes³⁷. A solution containing core-FGF21-LW displayed the initial optical density at 600 nm (OD_{600}) of 0.005 when incubated at 75 °C. However, over the duration of the treatment, the OD_{600} value of the solution reached 1.086, indicating that core-FGF21-LW formed aggregates. In contrast, the OD_{600} value of a solution containing core-FGF21 remained constant, which led us to assume that the β 10– β 12 loop is related to the heat response of FGF21 (Supplementary Fig. S3). Similar to the wild type, the loop-swapped FGF21 mutant with the N- and C-terminal loops (FGF21-LW) activated FGF receptor 1c (FGFR1c) (Fig. 3A), and its CD spectra in the far-UV region (190–260 nm) was similar to that of the wild type (Fig. 3B). Taken together, the loop replacement disturbed only the thermal behavior without affecting the structural and functional properties of FGF21.

Heat treatment purification of active human FGF21. *E. coli* is a mesophilic organism frequently used to produce recombinant proteins. Since most *E. coli* proteins are heat-labile, incubation at high temperatures is an efficient strategy for the purification of thermostable proteins produced in *E. coli*. As described in the “Materials and methods” section, heat treatment at 100 °C was implemented to purify FGF21. In our construct design, FGF21 was expressed with the N-terminal Trx tag. Since the tag is heat stable, the Trx-FGF21 fusion protein was incubated at 100 °C for 10 min³⁸, which separated the Trx-FGF21 protein from heat-labile *E. coli* proteins that precipitated at high temperatures³⁹ (Supplementary Fig. S4). Subsequently, the Trx tag was removed by the cleavage of the linker between the tag and FGF21 to secure only FGF21⁴⁰. According to DLS analysis, the size of FGF21 purified through heat treatment (htFGF21) was highly similar to that of FGF21 purified without heating (nFGF21) (Supplementary Fig. S5). This strongly suggests that heat treatment has little influence on the quality of FGF21⁴¹.

Our CD and DLS analyses revealed that heat treatment had little effect on the structure of FGF21 (Fig. 2, Supplementary Fig. S5). Therefore, we investigated whether heat treatment influences the activity of FGF21 by comparing FGFR1c/ β -Klotho activation levels of nFGF21, htFGF21, and commercial FGF21 (cFGF21) using FGF21-responsive reporter cells (modified HEK293 cells) that allow for monitoring FGFR1c/ β -Klotho activation.

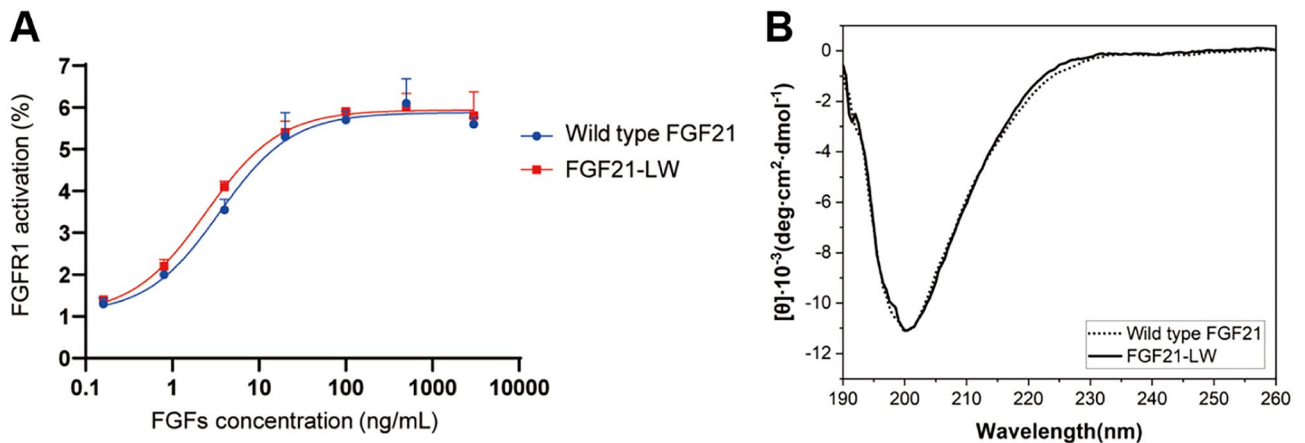


Figure 3. The maintenance of structural and functional properties of the loop-swapped FGF mutant. **(A)** Cell-based activity tests of FGF21-LW. Modified HEK293 cells for reporting FGFR1c activity were treated with the wild type FGF21 or FGF21-LW at the indicated concentration for 6 h. Cell lysates were prepared for detection of luciferase activity. The levels of FGFR1c activity in non-treated cells were set to 1, and the other values were calculated relative to this value ($n = 2$, average \pm SD). **(B)** Comparison of far-UV CD spectra between the wild type FGF21 and FGF21-LW.

Both nFGF21 and htFGF21 displayed little difference in FGFR1c/ β -Klotho activation levels, which were comparable to the activity of cFGF21 (Fig. 4A). Since adipocytes are one of the major targets of FGF21, we also examined the activities of the three FGF21s by detecting the phosphorylation of FGFR substrate 2 (FRS2) and extracellular signal-regulated kinase (ERK) in 3T3L1 adipocytes. The treatment of nFGF21, htFGF21, and cFGF21 led to similar phosphorylation levels of FRS2 and ERK (Fig. 4B,C). Furthermore, the levels of glucose uptake by FGF21s were similar in 3T3L1 adipocytes (Fig. 4D). These results indicate that FGF21 remains active after heating. Furthermore, we determined the rate constants for association (k_a) and for dissociation (k_d) of the wild type FGF21s for β -Klotho in ligand binding assay by SPR. The results showed that both nFGF21 and htFGF21 bind to β -Klotho with similar equilibrium dissociation constants (K_D) of 12.8 nM and 12.9 nM, respectively (Table 1, Supplementary Fig. S10).

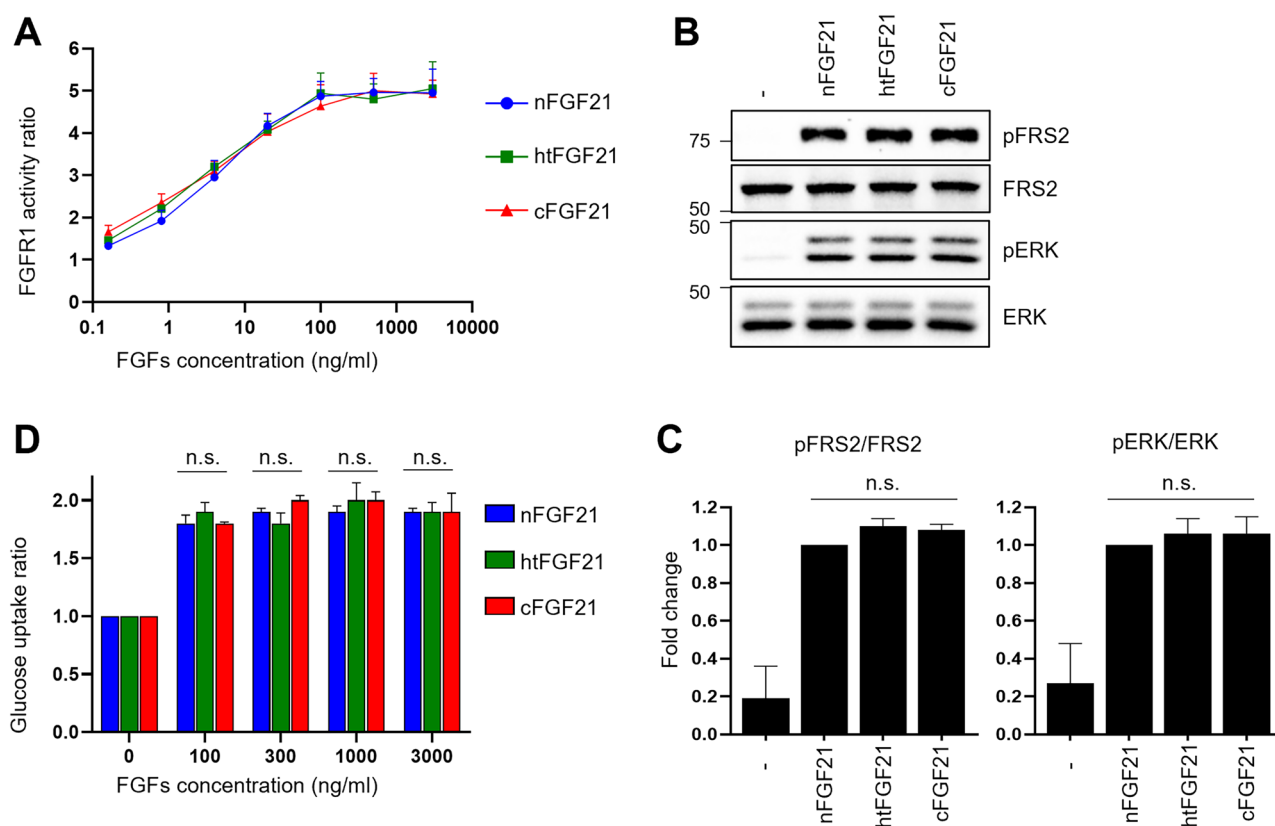


Figure 4. Cell-based activity tests of htFGF21. (A) Modified HEK293 cells used for reporting the FGFR1c/ β -Klotho activity was treated with nFGF21, htFGF21, or cFGF21 at the indicated concentration for 6 h. Cell lysates were prepared for detection of luciferase activity. The levels of FGFR1c activity in non-treated cells were set to 1, and the other values were calculated relative to this value ($n = 3$, average \pm SEM). (B) 3T3L1 adipocytes were treated with 100 ng/mL FGF21s for 15 min. Protein samples were prepared for western blotting. The original blots are presented in Supplementary Fig. S15. (C) The band density of nFGF21 treated cells was set to 1, and the other values were calculated relative to this value ($n = 3$, average \pm SEM). (D) 3T3L1 adipocytes were treated with FGF21s at the indicated concentration for 6 h, followed by detection of glucose uptake levels. The glucose uptake values of non-treated cells were set to 1, and the other values were calculated relative to this value ($n = 3$, average \pm SEM). The significance was evaluated using the one-way ANOVA, followed by Tukey's post hoc test. *n.s.* not significant.

	k_a ($10^4 \text{ M}^{-1} \text{ s}^{-1}$)	k_d (10^{-4} s^{-1})	K_D (nM)	Fold change of K_D s relative to nFGF21
nFGF21	12.6 \pm 1.8	15.9 \pm 0.3	12.8 \pm 1.6	–
htFGF21	12.1 \pm 1.1	15.5 \pm 0.5	12.9 \pm 0.8	0.99
htM2	12.0 \pm 0.8	13.0 \pm 0.4	10.9 \pm 0.5	1.17
htM3	15.2 \pm 0.9	7.85 \pm 0.2	5.19 \pm 0.3	2.47
htM5	16.4 \pm 0.7	7.07 \pm 0.2	4.32 \pm 0.1	2.96

Table 1. Kinetic rate constants for β -Klotho as determined by SPR. The values were represented by mean \pm SD for three independent experiments that were each fit.

The administration of human or murine FGF21 alleviates the progression of NAFLD in HFD-induced obesity models^{42–45}. Considering that nFGF21 has traditionally been used in those previous studies, we sought to determine whether htFGF21 was also effective in ameliorating fatty liver. To investigate the effects of htFGF21 on NAFLD, HFD-fed mice were intraperitoneally injected with 1 or 10 mg/kg htFGF21, once daily for 14 days. The injections of either 1 or 10 mg/kg htFGF21 markedly reduced body weight in HFD-fed mice compared with vehicle controls (Fig. 5A,B). Significant increases in intrahepatic TG contents were observed in vehicle-treated HFD-fed mice compared with vehicle-treated NCD-fed mice; however, the HFD-induced increases in intrahepatic TG dramatically diminished after treatment with 1 or 10 mg/kg htFGF21 (Fig. 5C). Histological analyses of liver tissue stained with hematoxylin and eosin (H&E) showed that there was extensive hepatocyte vacuolation in vehicle-treated HFD-fed mice, suggesting intrahepatic fat accumulation (Fig. 5D). Conversely, few hepatocellular vacuolations were observed in liver sections of either 1 or 10 mg/kg htFGF21-treated HFD-fed mice, which was comparable with that of vehicle-treated NCD-fed mice (Fig. 5D). Moreover, Oil red O staining of liver sections showed that htFGF21 injections dramatically attenuated the formation of intense lipid droplets in HFD-fed mice (Fig. 5D). These results suggest that htFGF21 treatment can prevent HFD-induced NAFLD in mice. Collectively, cell-based functional assays and in vivo mouse model studies strongly suggest that heating allows for an easy and effective purification of active FGF21.

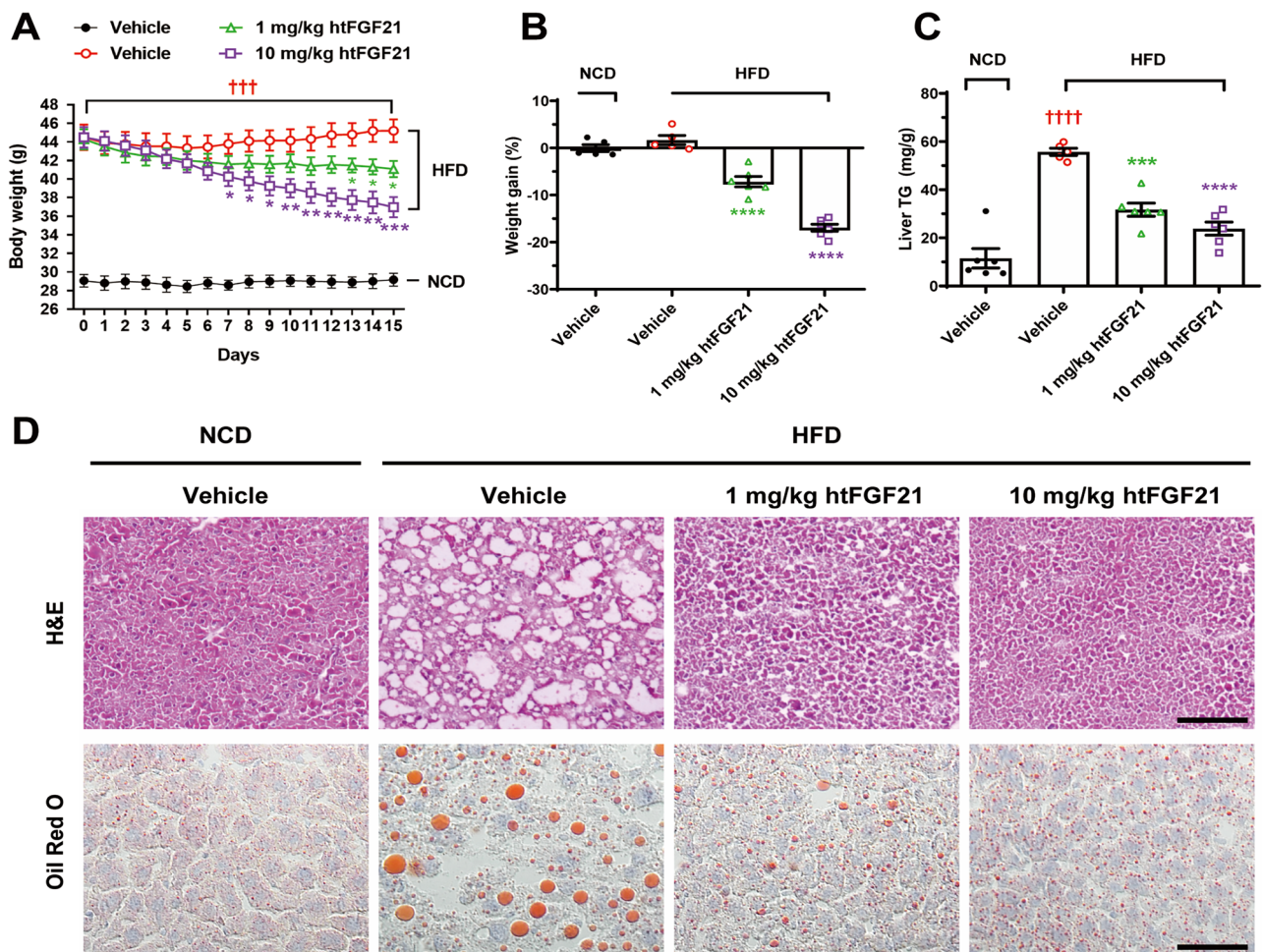


Figure 5. In vivo activity tests of htFGF21. HFD-fed mice were injected with htFGF21 intraperitoneally at doses of 0 (vehicle), 1, or 10 mg/kg once daily for 14 days. NCD-fed mice were included as controls and injected intraperitoneally with vehicles. **(A)** Changes in body weight throughout the injection. **(B)** Percent weight gains on the following day after the last injection. **(C)** Effects of the injection on liver TG contents. **(D)** H&E and Oil Red O staining of liver sections showing reversal of vacuolation and lipid accumulation in htFGF21-injected HFD-fed mice. Data are represented as mean \pm SEM, calculated using one-way ANOVA followed by Tukey's multiple comparisons test, * $p < 0.05$, ** $p < 0.01$, *** and ††† $p < 0.001$, **** and †††† $p < 0.0001$. $n = 5\text{--}6$ mice/group. ††† and †††† indicate vehicle-injected NCD-fed mice versus vehicle-injected HFD-fed mice. *, **, ***, and **** indicate vehicle-injected HFD-fed mice versus htFGF21-injected HFD-fed mice. Scale bars: 100 μm (H&E), 50 μm (Oil Red O).

Structure-based design of a FGF21 mutant with enhanced potency. According to the crystal structure of the C-terminal loop of human FGF21 complexed with β -Klotho^{11,12}, residues at positions 201 and 208 are directly involved in interactions with β -Klotho; the side chains of Gln201 and Ala208 fit into a small pocket and canyon, respectively, on the surface of β -Klotho (Supplementary Fig. S7). Sequence comparison shows that Gln201 and Ala208 of human FGF21 are replaced by His201 and Thr208, respectively, in some mammalian FGF21s (Supplementary Fig. S8). It is notable that regions of β -Klotho interacting with the residues at positions 201 and 208 of FGF21 (Gln201/His201 and Ala208/Thr208) were highly conserved in mammalian β -Klotho (Supplementary Fig. S9). To assess the effects of the two amino acids replacements, we introduced Q201H and A208T mutations into the C-terminal loop of FGF21. The htFGF21 variant with Q201H and A208T mutations (htM2) displayed 2-fold increased potency for FGFR1c/ β -Klotho activation than the wild type htFGF21 (Fig. 6A).

In terms of the structural aspect, the C-terminal loop protrudes from the main body of FGF21 and thus is vulnerable to proteolytic degradation. Fibroblast activation protein (FAP) in serum inactivates FGF21 by cleaving the peptide bond between Pro199 and Ser200 in the C-terminal loop, and the P199G mutation is effective to prevent the FAP-mediated cleavage of the loop³¹. With a rationale that the enhanced flexibility of the C-terminal loop can have a positive effect on β -Klotho binding⁴⁶, we introduced two more glycines to the C-terminal loop (S195G and S200G) in addition to the P199G mutation. In the crystal structure of the C-terminal loop complexed with β -Klotho¹¹, the side chains of both serine residues are exposed to the solvent without interacting with β -Klotho (Supplementary Fig. S7). Therefore, the Ser \rightarrow Gly mutations are likely to have no effect on β -Klotho interactions but could increase the loop flexibility. The htFGF21 variant with S195G, P199G, and S200G mutations (htM3), which has three glycine residues in the C-terminal loop, showed 3.65-fold higher potency for FGFR1c/ β -Klotho activation than the wild type htFGF21 (Fig. 6A).

Encouraged by the two mutational studies that produced mutant FGF21s with higher FGFR1c/ β -Klotho-activating functions, we combined the five point-mutations in the C-terminal loop. The htFGF21 variant with S195G, P199G, S200G, Q201H, and A208T mutations (htM5) showed the highest potency for FGFR1c activation;

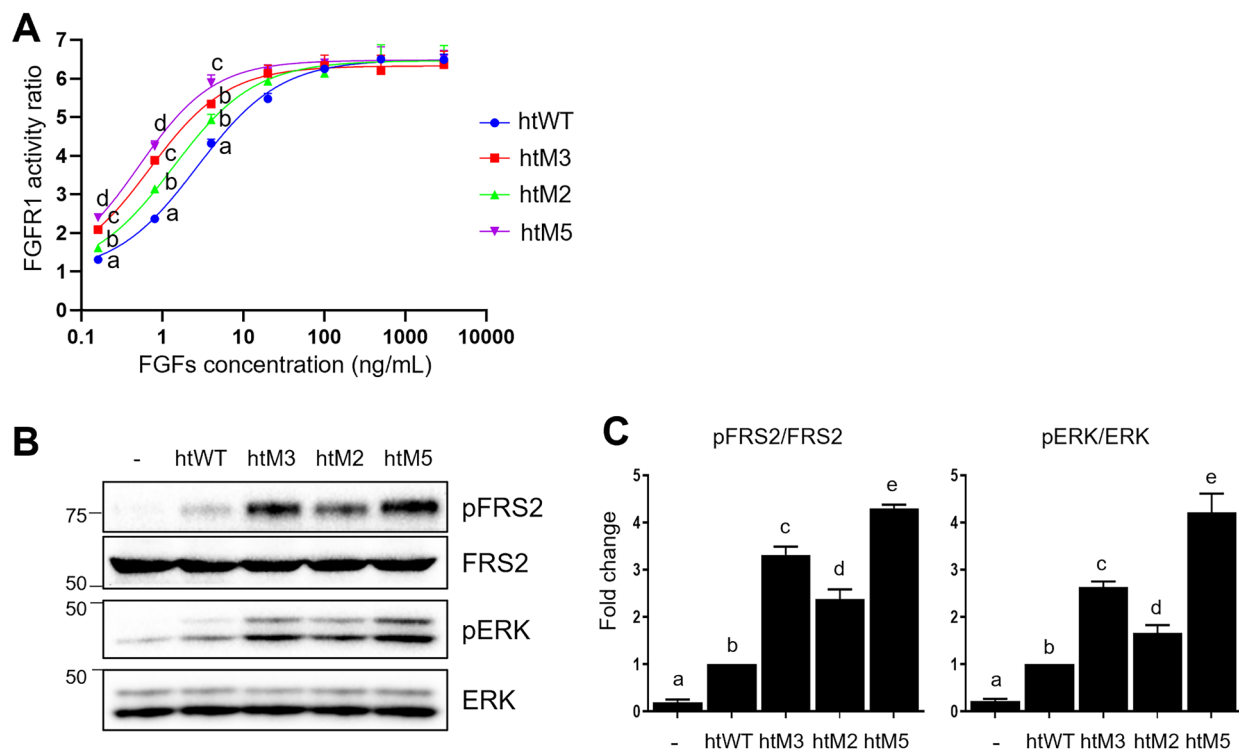


Figure 6. Cell-based activity tests of htM2, htM3, and htM5. (A) Modified HEK293 cells used for reporting FGFR1c/ β -Klotho activity was treated with the wild type htFGF21 (htWT), htM2, htM3, and htM5 at the indicated concentration for 6 h. Cell lysates were prepared for detection of luciferase activity. The levels of FGFR1c/ β -Klotho activity in non-treated cells were set to 1, and the other values were calculated relative to this value ($n = 4$, average \pm SEM). Non-linear regression was performed using GraphPad Prism 8, and the best-fit non-linear regression curve is depicted. EC_{50} s of htWT, htM2, htM3, and htM5 were calculated as 2.74 ± 0.24 , 1.37 ± 0.06 , 0.75 ± 0.17 , and 0.52 ± 0.01 ng/mL (average \pm SEM), respectively. The statistical differences at each concentration were evaluated using one-way ANOVA followed by Tukey's post hoc test and are represented as a, b, c, and d. $p < 0.05$. (B) 3T3L1 adipocytes were treated with htWT, htM2, htM3, and htM5 30 ng/mL for 15 min. Protein samples were prepared for western blotting. The original blots are presented in Supplementary Fig. S15. (C) The band density of htWT treated cells was set to 1, and the other values were calculated relative to this value ($n = 3$, average \pm SEM). Statistical significance was evaluated using one-way ANOVA followed by Tukey's post hoc test and was marked as a, b, c, d, and e. $p < 0.05$.

this htM5 mutant showed 5.27-fold higher potency than the wild type htFGF21 (Fig. 6A). The activities of htM2, htM3, and htM5 were also confirmed in 3T3L1 adipocytes. Consistent with FGFR1c/ β -Klotho activation in Fig. 6A, the three mutants increased the levels of phosphorylated FRS2 and ERK more than the wild type htFGF21 (Fig. 6B,C). We performed SPR assays to examine the influence of the five point-mutations in the C-terminal loop on β -Klotho binding. The K_D value of htM2 (10.9 nM) was slightly higher than that of the wild type htFGF21 (12.8 nM) and htFGF21 (12.9 nM) (Table 1, Supplementary Fig. S10). In the case of htM3 and htM5, they exhibited 2.47- and 2.96-fold higher affinities to β -Klotho than wild type FGF21s; their K_D values were 5.19 nM and 4.32 nM, respectively (Table 1, Supplementary Fig. S10). Compared to wild type FGF21s, both mutants displayed similar k_a and lower k_d , indicating that slow dissociation is the cause of their tight binding to β -Klotho (Table 1, Supplementary Fig. S10).

To compare effects on NAFLD between the wild type and htM5, HFD-fed mice were intraperitoneally injected with 0.1 or 0.5 mg/kg of htFGF21 or htM5, once daily for 14 days. Although the injections of either the 0.1 mg/kg htFGF21 or htM5 decreased body weight compared with vehicle-treated mice, the trend for body weight loss was greater in the htM5 group than in the htFGF21 group (Fig. 7A,B). Mice injected with either the 0.5 mg/kg htFGF21 or htM5 treatment showed significant body weight loss compared with vehicle-treated mice, and there was no difference in the extent of weight loss between the htFGF21 and htM5 groups (Fig. 7A,B). Either the htFGF21 or htM5 injections substantially reduced hepatic TG content in a dose-dependent manner but htM5 significantly decreased hepatic TG content more than htFGF21 at 0.1 mg/kg (Fig. 7C).

Although the vacuolization was still observed in the both livers of mice injected with 0.1 mg/kg of the htFGF21 or htM5, the degree of vacuolization was reduced compared with vehicle-injected mice and the effect of htM5 was greater than that of htFGF21 (Fig. 7D). Similarly, Oil red O staining revealed that either the htFGF21 or htM5 administration suppressed HFD-induced hepatic lipid accumulation. htM5 inhibited lipid accumulation

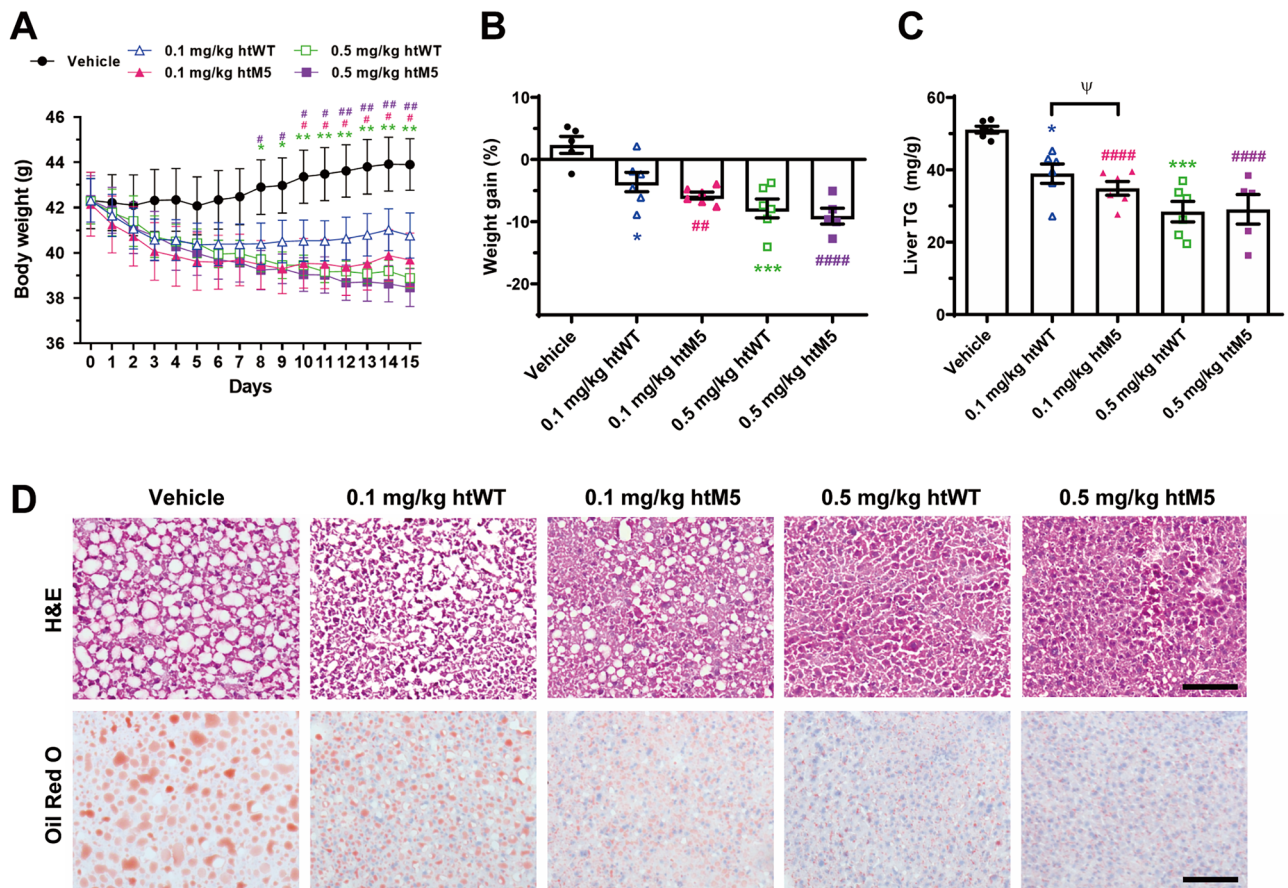


Figure 7. In vivo activity tests of htM5. HFD-fed mice were injected with the wild type htFGF21 (htWT) or htM5 intraperitoneally at doses of 0.1 or 0.5 mg/kg once daily for 14 days. (A) Changes in body weight throughout the injection. (B) Percent weight gains on the following day after the last injection. (C) Effects of the injection on liver TG contents. (D) H&E and Oil Red O staining of liver sections showing better improvement in htM5 than htWT for the vacuole and lipid accumulation. Data are represented as mean \pm SEM, calculated using two-way ANOVA followed by Tukey's multiple comparisons test, *, #, and $\Psi p < 0.05$, ** and $\#p < 0.01$, *** $p < 0.001$, #### $p < 0.0001$. $n = 5-6$ mice/group. *, **, and *** indicate vehicle-injected mice versus the htWT-injected mice. #, ##, and #### indicate vehicle-injected mice versus the htM5-injected mice. Ψ indicates the htWT-injected mice versus the htM5-injected mice. Scale bars: 100 μ m (H&E), 50 μ m (Oil Red O).

at a higher degree than htFGF21 at the dose of 0.1 mg/kg (Fig. 7D). Taken together, these results suggest that the introduction of five point-mutations gave rise to the htM5 mutant that is likely to exert better effects for ameliorating NAFLD than the wild type.

Discussion

Characterization of protein stability is an integral step in biopharmaceutical development⁴⁷ and the monitoring of thermal behavior is a classical probe to investigate protein stability⁴⁸. To examine temperature-dependent structural changes of FGF21, we performed CD experiments. The CD spectra of FGF21 can be roughly grouped into three distinct states depending on temperatures; CD spectra between 20 and 40 °C, at 60 °C, and between 80 and 100 °C (Fig. 2A,C). This observation is compatible with the previous report about three thermal unfolding states of FGF21 detected by differential scanning calorimetry⁴⁹. Remarkably, we discovered the temperature-responsive structural reversibility of FGF21 (Fig. 2E). The β 10– β 12 loop was identified to be associated with this remarkable thermal behavior; the loop replacement only perturbed thermal response of FGF21 without affecting structural and functional properties (Fig. 3, Supplementary Fig. S3). These ever-first findings led us to employ heating as an efficient purification step to separate recombinant FGF21 from heat-labile proteins (Supplementary Figs. S4, S6). It should be noted that heat treatment has no influence on the structure and function of FGF21 (Fig. 4, Supplementary Fig. S5). Heating has another advantage to prevent the proteolytic cleavage of the essential but fragile C-terminal loop of FGF21 during purification, since heat-labile host proteases lose their activities due to thermal denaturation. On SDS-PAGE, FGF21 purified with heating displayed no degradation whereas there was degradation pattern in the case of FGF21 purified without heating (Supplementary Fig. S6). Consequently, heating-based strategy can be widely applied for the purification of FGF21 analogs that are under therapeutic development.

FGF21 is targeted to cells and tissues harboring the tissue-specific transmembrane co-receptor β -Klotho and then forms the ternary signaling complex with β -Klotho and receptors^{15,16}. The C-terminal loop (residues 186–209) of FGF21 is responsible for interacting with β -Klotho. We introduced five point-mutations into the C-terminal loop to generate the M5 variant with high affinity to β -Klotho (Table 1) and enhanced potency in activation of FGF21 signaling (Figs. 6, 7). Consistently, this mutant displayed therapeutic potential in terms of body weight loss, the levels of hepatic triglycerides and lipids, and the degree of vacuolization of liver in high-fat diet-induced obesity mice (Fig. 7). Among the five mutations, S195G, S200G, Q201H, and A208T are firstly reported in this study whereas P199G is a well-known mutation to escape the proteolytic attack by a serum protease, FAP^{28–31}.

Q201H and A208T were designed based on sequence comparison (Supplementary Fig. S8), indicating that amino acid substitutions at non-conserved sequence positions among FGF21 orthologs can be used to design FGF21 variants. According to the crystal structure of the complex between β -Klotho and the C-terminal loop bearing the A208E mutation¹¹ (the FGF21-C/ β -Klotho structure), the side chain of Gln201 is accommodated in a pocket surrounded by Arg696, His743, Phe764, Glu768, Arg829, Arg845, and Phe849 (Supplementary Fig. S7). Histidine and glutamine are similar amino acids in terms of volume and hydrophathy. The volume of histidine and glutamine are 153.2 Å³ and 143.8 Å³, respectively, while the hydrophathy scale of histidine and glutamine are –3.2 and –3.5, respectively⁵⁰. Consequently, the Q201H mutation, which locates a bit larger and a bit more neutral amino acid into the pocket, seems to allow for better contact between the imidazole side chain of histidine and the residues lining the pocket.

In the FGF21-C/ β -Klotho structure¹¹, Glu208 is located in a canyon and its side chain is sandwiched between His646 and Pro940 of β -Klotho. The hydrophobic hydrocarbon chain of Glu208 contacts with Pro940 and its terminal carboxylate group interacts with the imidazole side chain of His646 (Supplementary Fig. S7). The side chain of threonine has both a hydrophobic methyl group and a polar hydroxyl group whereas alanine only has a hydrophobic methyl side chain. Therefore, threonine seems to be more suitable for position 208 than alanine since its side chain is able to form favorable interactions with His646 and Pro940. In the case of the side chains of Ser195 and Ser200, they have no interactions with β -Klotho, an indication of little contribution of their side chains to β -Klotho binding. Therefore, the glycine introduction instead of serine seems to be beneficial for co-receptor binding due to the increased flexibility of the C-terminal loop.

The functional consequences of each position in the C-terminal sequences have been elaborately examined through peptide-based alanine scanning at a single amino acid resolution⁵¹, in which the alanine substitutions at the five mutation positions presented here were suggested to have little effect on β -Klotho binding. The enhanced potency of the M5 variant harboring the five point-mutations (S195G, P199G, S200G, Q201H, and A208T) shows that the introduction of non-alanine amino acids at the inert positions and their synergistic combinations could lead to the development of FGF21 variants with improved therapeutic potential.

To estimate whether the five point-mutations affect immunogenicity, we analyzed the binding affinity of peptides derived from the C-terminal loop (residues 174–209) in the wild type FGF21 and M5 towards major histocompatibility complex (MHC) molecules of T cell by using TepiTool⁵² in Immune Epitope Database (IEDB). According to this analysis where binding affinities were represented by IC₅₀ values, most peptides from both proteins were predicted to have high IC₅₀ values, suggesting little binding to MHC molecules^{53–55} (Supplementary Figs. S11, S12). Furthermore, the peptide “GMVGGGHGR” of M5 harboring four mutations (S195G, P199G, S200G, and Q201H in thick letters) has significantly higher IC₅₀ values (~353 nM) towards some MHC class I alleles than the corresponding “SMVGPSQGR” peptide of the wild type (IC₅₀ of 91–200 nM) (Supplementary Fig. S11). We also performed B cell epitope predictions for the C-terminal loop of the wild type FGF21 and M5 using ‘Kolaskar and Tongaonkar antigenicity’⁵⁶ and ‘Bepipred linear epitope prediction 2.0’^{57,58} tools available at IEDB. In these analyses, residues with higher scores than the threshold can be considered to be immunogenic. As shown in Supplementary Fig. S13, the region of M5 harboring the five-point mutations have less scores than

the corresponding region of the wild-type, which together with the T cell epitope prediction, indicates that the M5 variant is highly likely to be at most as immunogenic as the wild type.

Materials and methods

Cloning, expression, and heat-treatment-mediated purification of human FGF21. The coding genes of the wild type FGF21 (residues 33–209), the β -trefoil region of FGF21 (residues 41–173; core-FGF21), and all FGF21 variants (FGF21-LW, core-FGF21-LW, M2, M3, and M5; see the “Results and Discussion” sections) were synthesized using a TEV protease cleavage site (ENLYFQ/G) at the N-terminus (COSMOGENETECH, Republic of Korea). The synthesized genes were inserted at the *Bam*HI and *Sal*I sites of the expression vector pET32a (+) (Novagen, Darmstadt, Germany) to fuse thioredoxin (Trx) to the N-terminus of the target proteins. They were transformed into *Escherichia coli* strain Rosetta (DE3). The transformants were grown to an OD₆₀₀ of 0.6–0.7 in Luria–Bertani (LB) media containing 50 μ g/mL ampicillin and chloramphenicol at 37 °C, and 0.5 mM isopropyl-D-thiogalactoside (IPTG) was added for the expression of the Trx-fused target proteins.

After 42 h of incubation at 15 °C, cells were harvested using centrifugation, resuspended in a buffer (10 mM Tris pH 8.0 and 200 mM NaCl), and disrupted using sonication. To remove cellular debris, centrifugation was performed at 10,000 \times g for 40 min at 4 °C. The supernatant was heated at 100 °C for 10 min in a water bath and subsequently centrifuged to secure only soluble fractions. The heat-treated soluble fractions were loaded into a nickel-nitrilotriacetic acid column (GE Healthcare, Marlborough, MA, USA) and incubated with ~0.3 mg/mL TEV protease overnight at 22 °C to detach target proteins from the Trx tag bound to the resin. The unbound fractions containing target proteins were applied to the Q Sepharose® Fast Flow column (GE Healthcare) equilibrated with A buffer (10 mM Tris pH 8.0). The elution was performed using a linear gradient of 0–1.0 M NaCl. The fractions containing target proteins were finally loaded onto a HiLoad® 16/600 Superdex® 75 pg column (GE Healthcare) equilibrated with a buffer consisting of 10 mM NaH₂PO₄ (pH 8.0) and 200 mM NaCl. Purification was performed by using the AKTA-FPLC system (GE Healthcare, Marlborough, MA, USA). Proteins used for circular dichroism (CD), dynamic light scattering (DLS), and spectrophotometry were purified without heat treatment. Commercial FGF21 (cat# CYT-474) was purchased from ProSpec, Israel.

Cloning, expression, and purification of human FGF2. The coding gene of FGF2 (residues 143–288) was synthesized at the *Nde*I and *Xho*I sites of the expression vector pET17b (+) (Novagen). The resulting construct was transformed into Rosetta (DE3) pLysS. The transformant was grown to an OD₆₀₀ of 0.6–0.7 in LB media containing 50 μ g/mL ampicillin and chloramphenicol at 37 °C, and 0.5 mM IPTG was added. After 20 h of incubation at 20 °C, cells were harvested using centrifugation, resuspended in a buffer (10 mM Tris pH 8.0 and 200 mM NaCl), and disrupted using sonication. To remove cellular debris, centrifugation was performed at 10,000 \times g for 40 min at 4 °C. The soluble fractions were loaded into a heparin column (GE Healthcare) and eluted using a linear gradient of 0.5–2.0 M NaCl in 10 mM Tris pH 8.0 buffer. The fractions containing target proteins were collected and finally loaded onto a HiLoad® 16/600 Superdex® 75 pg column (GE Healthcare) equilibrated with a buffer consisting of 10 mM NaH₂PO₄ (pH 8.0) and 200 mM NaCl. Purification was performed using the AKTA-FPLC system (GE Healthcare).

Circular dichroism spectroscopy. CD experiments were performed using a Jasco J-1500 equipped with Jasco PTC-517 Peltier cell holder, a thermostat (Jasco Corporation, Tokyo, Japan). CD spectra were collected with a scanning speed of 50 nm/min, a digital integration time of 4 s, and a bandwidth of 1 nm. Quartz cuvettes with a path length of 1 mm were employed. The signal of a protein-free buffer containing 10 mM NaH₂PO₄ (pH 8.0) and 20 mM NaCl was subtracted from all CD spectra. Each spectrum, an average of 5 scans, was normalized to molar ellipticity (θ) using the mean weight residue and concentration by using a program provided by the manufacturer.

To monitor the thermal denaturation, CD spectra of 0.2 mg/mL proteins were collected every 1 °C at 215 nm as the temperature was changed from 20 to 100 °C with a heating rate of 1 °C/min. Spectral curves were fitted using the OriginPro 2021 program (Origin Lab Corporation, Northampton, MA, USA) through a non-linear adjustment by the Boltzmann method. When temperature reached 20, 40, 60, 80, and 100 °C during the thermal denaturation experiments, the far-UV CD spectra were obtained in the range of 190–260 nm. The near-UV CD spectra were obtained in the range of 240–340 nm using 5 mg/mL of proteins. Heating rate was set at 5 °C/min and the temperature was maintained for 10 min at 20, 40, 60, 80, and 100 °C. The far- and near-UV CD spectra were collected by continuous scanning at 0.5 nm intervals. The structural reversibility was checked by stepwise cooling of the protein solution from 100 to 20 °C.

Turbidity measurement. The optical density at a wavelength of 600 nm was measured at 75 °C using the V-730 UV–Vis Spectrophotometer (Jasco Corporation) equipped with a bath circulator. The concentration of proteins in a buffer consisting of 10 mM NaH₂PO₄ (pH 8.0) and 200 mM NaCl was 25 mg/mL. The value of optical density was determined by subtracting the signal of the protein-free buffer. Measurements began 15 s after putting samples into the spectrophotometer.

Dynamic light scattering. DLS experiments were conducted at 20 °C using a Zetasizer Nano ZS apparatus (Malvern Instruments Ltd., Malvern, UK) by setting an automatic attenuator. Proteins having a concentration of 25 mg/mL in a buffer consisting of 10 mM NaH₂PO₄ (pH 8.0) and 200 mM NaCl were centrifuged at 13,000 rpm for 15 min at 4 °C. The supernatant was transferred to a glass cuvette having a path length of 1 cm that was located at a position of 4.65 mm. The light scattering intensities were collected 14 times at an angle of 173° using

a 10 s acquisition time. The size distributions of the target proteins were calculated using the correlation functions by employing the “general purpose mode” in a Zetasizer software v7.13 (Malvern Instruments Ltd.).

Surface plasmon resonance assay. The experiments were employed by Biacore 8 K system (GE Healthcare). The interactions were studied at 25 °C in HBS-EP + buffer (10 mM HEPES, pH 7.4, 150 mM NaCl, 3 mM EDTA, and 0.05% (v/v) polysorbate 20; Cytiva, Marlborough, MA, USA). FGF21s were covalently immobilized on research-grade CM5 sensor chip (Cytiva) using amine coupling kit (cat# BR100050; Cytiva) at surface densities of approximately 700–900 response units (RU). Human β -Klotho (cat# 5889-KB-050; R&D Systems) was diluted as 2.5-fold series (250, 100, 40, 16, 6.4, 2.56, 1.024, and 0 nM) in running buffer and injected over the sensor chip at a flow rate of 30 μ l/min. Contact and dissociation was monitored for 300 s. Between each cycle, the chip surface was regenerated by a buffer consisting of 10 mM Glycine-HCl (pH 1.5) for 30 s. The data were processed with the Biacore Insight Evaluation software (GE Healthcare). The kinetic parameters (k_a , k_d , and K_D) were calculated by a global fitting analysis assuming a Langmuir binding model at 1:1 stoichiometry.

FGFR1c/ β -Klotho activity assay. To determine the activation level of FGFR1c/ β -Klotho by FGF21, we used the iLite[®] FGF-21 assay ready cells (cat# BM3071; SVAR, Malmo, Sweden). These are HEK293 cells modified to express FGFR1c, β -Klotho, GAL4 DNA binding domain fused trans-activation domain of Elk1, GAL4 DNA binding sequence contained reporter gene (firefly luciferase), and renilla luciferase. Cells were seeded with a different concentration of FGF21 proteins in 96-well plates and incubated at 37 °C in a humidified 5% CO₂ incubator. After 6 h, luciferase activity was determined using the Dual-Glo luciferase assay system (E2920; Promega, Madison, WI, USA) and GloMax[®]96 microplate luminometer (Promega).

Cell culture and glucose uptake assay. 3T3L1 preadipocytes were incubated in Dulbecco’s modified Eagle’s medium (DMEM; GIBCO, Life Technologies Ltd., Paisley, UK) supplemented with 10% bovine serum (GIBCO) and 1% penicillin/streptomycin (GIBCO) at 37 °C in a humidified 5% CO₂ incubator. Two days after cells had reached confluence, adipogenesis was stimulated. Cells were maintained in DMEM containing 10% fetal bovine serum (FBS; GIBCO), 0.5 mM IBMX, 0.25 μ M DEX, and 5 μ g/mL insulin for 2 days. Next, cells were incubated in DMEM containing 10% FBS and 1 μ g/mL insulin. After 2 days, cells were maintained in DMEM containing 10% FBS for 4 days. Cellular glucose uptake was determined using the Glucose Uptake-Glo[™] Assay (J1342; Promega). Briefly, cells were incubated with FGF21 proteins for 6 h in growth media, followed by incubation in glucose- and serum-free DMEM for 30 min. Cells were treated with 2-deoxyglucose for 10 min. Next, we measured the level of accumulated 2-deoxyglucose-6-phosphate (2DG6P) using the assay kit according to the manufacturer’s protocol using a GloMax[®]96 microplate luminometer (Promega).

Western blot analysis. To determine FGFR signaling, 3T3-L1 cells were incubated in serum-free DMEM. After 1 h, cells were treated with FGF21 proteins for 15 min. Protein samples were prepared using lysis buffer containing 20 mM Tris-HCl (pH 7.4), 1% NP-40, 10 mM Na₄P₂O₇, 100 mM NaF, 2 mM Na₃VO₄, 5 mM EDTA, and a protease inhibitor cocktail (#87786; ThermoFisher Scientific, MA, USA). Whole cell lysates (20 μ g) were subjected to SDS-PAGE and immunoblotted with specific antibodies against pFRS2a (#3864; Cell signaling Technology, Beverly, MA, USA), FRS2 (sc-17841; Santa Cruz Biotech, Santa Cruz, CA, USA), pERK (#4370; Cell signaling Technology), and ERK (#4696; Cell signaling Technology). Membranes were cut according to the target protein size, and then they were hybridized with specific antibodies. Blots were developed using Clarity[™] Western ECL Blotting Substrates (Bio-Rad, Hercules, CA, USA), ECL-Prime (ThermoFisher Scientific), or EZ-Western Lumi Fento (DoGen, Seoul, Korea) with a ChemiDoc Imaging System (Bio-Rad).

Animals and treatments. All animal experiments were conducted in accordance with the guidelines on animal care including the ARRIVE guidelines and use as approved by the Institutional Animal Care and Use Committee of Daegu Gyeongbuk Institute of Science and Technology (DGIST-IACUC-19121001-0001). Male C57BL/6 mice at 7 weeks of age were purchased from Koatech. Mice were housed under a 12 h light/12 h dark cycle (lights on from 7:00 am to 7:00 pm) in individually ventilated cages (1 mouse per cage) with chip bedding at 23 °C \pm 3 °C and a relative humidity of 50% \pm 10%. Before the HFD experiments, mice were acclimated to the housing facility for 1 week and given ad libitum access to water and normal chow diet (NCD) (12% kcal from fat; Lab Supply, 5053). After 10 weeks of a NCD or HFD (60% kcal from fat; Envigo, 06414) treatment, HFD-fed mice were randomly assigned to vehicle or FGF21 treatment groups. The randomization was stratified by body weight. The NCD-fed mice were intraperitoneally injected with vehicle (DPBS, 21-031-CV; Corning, NY, USA) and the HFD-fed mice were intraperitoneally injected with vehicle, wild type FGF21, or mutant FGF21 once daily for 2 weeks. All mice had free access to water and food while remaining on their respective diets during the drug treatment periods. The single injection was performed between 4:00 pm and 6:00 pm, and body weight and food consumption were measured immediately before each injection every day. The following day after the last injection, mice were sacrificed to collect livers after noting final measurements.

Liver TG quantification. Hepatic TG content was measured using Triglyceride Quantification Colorimetric/Fluorometric Kit (K622-100; BioVision, Milpitas, CA, USA). Livers were homogenized in 1 mL of a solution containing 5% NP-40 in water, heated to 80–100 °C, and allowed to cool to room temperature; this step was repeated twice. Insoluble material was removed using centrifugation at 16,000 \times g for 2 min. Extracted TG was diluted sixfold with distilled water. TG level was measured according to the manufacturer’s instructions. Individual TG levels were normalized to liver weight.

Liver histology. Histological analyses of the NAFLD tissues were performed using the H&E Stain Kit (Hematoxylin and Eosin) (ab245880; Abcam, Cambridge, UK) and the Oil Red O Stain Kit (Lipid Stain) (ab150678; Abcam). Each staining was performed according to the manufacturers' protocols with minor modifications. Livers were rapidly excised from mice, embedded in FSC 22 Frozen Section Media (3801480; Lecia Biosystems, Nussloch, Germany), and frozen on dry ice. Next, fresh frozen sections were obtained on a cryostat (CM3050S; Lecia Biosystems) and fixed using ice cold 4% paraformaldehyde solution (p2031; Biossang, Seongnam, Korea) for 15 min. The sections were cut into 5 and 7 μm sections for H & E and Oil Red O staining, respectively. Histological sections of livers were assessed blindly for pathological changes.

Data availability

The datasets are available from the corresponding author on reasonable request.

Received: 25 February 2022; Accepted: 6 January 2023

Published online: 18 January 2023

References

- Xie, Y. *et al.* FGF/FGFR signaling in health and disease. *Signal Transduct. Target. Ther.* **5**, 181 (2020).
- Ornitz, D. M. & Itoh, N. The fibroblast growth factor signaling pathway. *WIREs Dev. Biol.* **4**, 215–266 (2015).
- Ornitz, D. M. & Itoh, N. Fibroblast growth factors. *Genome Biol.* **2**, 3005 (2001).
- Longo, L., Lee, J. & Blaber, M. Experimental support for the foldability–function tradeoff hypothesis: Segregation of the folding nucleus and functional regions in fibroblast growth factor-1. *Protein Sci.* **21**, 1911–1920 (2012).
- Itoh, N. & Ornitz, D. M. Evolution of the Fgf and Fgfr gene families. *Trends Genet.* **20**, 563–569 (2004).
- Zhou, W.-Y., Zheng, H., Du, X.-L. & Yang, J.-L. Characterization of FGFR signaling pathway as therapeutic targets for sarcoma patients. *Cancer Biol. Med.* **13**, 260–268 (2016).
- Xu, R. *et al.* Diversification of the structural determinants of fibroblast growth factor–heparin interactions: Implications for binding specificity*. *J. Biol. Chem.* **287**, 40061–40073 (2012).
- Goetz, R. *et al.* Molecular insights into the Klotho-dependent, endocrine mode of action of fibroblast growth factor 19 subfamily members. *Mol. Cell. Biol.* **27**, 3417 (2007).
- Degriolamo, C., Sabbà, C. & Moschetta, A. Therapeutic potential of the endocrine fibroblast growth factors FGF19, FGF21 and FGF23. *Nat. Rev. Drug Discov.* **15**, 51–69 (2016).
- Chen, G. *et al.* α -Klotho is a non-enzymatic molecular scaffold for FGF23 hormone signalling. *Nature* **553**, 461–466 (2018).
- Lee, S. *et al.* Structures of β -klotho reveal a 'zip code'-like mechanism for endocrine FGF signalling. *Nature* **553**, 501–505 (2018).
- Kuzina, E. S. *et al.* Structures of ligand-occupied β -Klotho complexes reveal a molecular mechanism underlying endocrine FGF specificity and activity. *Proc. Natl. Acad. Sci.* **116**, 7819 (2019).
- Yie, J. *et al.* FGF21 N- and C-termini play different roles in receptor interaction and activation. *FEBS Lett.* **583**, 19–24 (2009).
- Kurosu, H. & Kuro-o, M. Endocrine fibroblast growth factors as regulators of metabolic homeostasis. *BioFactors* **35**, 52–60 (2009).
- Kurosu, M. The Klotho proteins in health and disease. *Nat. Rev. Nephrol.* **15**, 27–44 (2019).
- Kurosu, H. *et al.* Tissue-specific expression of Klotho and fibroblast growth factor (FGF) receptor isoforms determines metabolic activity of FGF19 and FGF21. *J. Biol. Chem.* **282**, 26687–26695 (2007).
- Kharitonov, A. *et al.* FGF-21/FGF-21 receptor interaction and activation is determined by β Klotho. *J. Cell. Physiol.* **215**, 1–7 (2008).
- Suzuki, M. *et al.* β Klotho is required for fibroblast growth factor (FGF) 21 signaling through FGF receptor (FGFR) 1c and FGFR3c. *Mol. Endocrinol.* **22**, 1006–1014 (2008).
- Adams, A. C., Cheng, C. C., Coskun, T. & Kharitonov, A. FGF21 requires β klotho to act in vivo. *PLoS ONE* **7**, e49977 (2012).
- Ogawa, Y. *et al.* β Klotho is required for metabolic activity of fibroblast growth factor 21. *Proc. Natl. Acad. Sci.* **104**, 7432 (2007).
- Kharitonov, A. *et al.* FGF-21 as a novel metabolic regulator. *J. Clin. Invest.* **115**, 1627–1635 (2005).
- Talukdar, S. *et al.* A long-acting FGF21 molecule, PF-05231023, decreases body weight and improves lipid profile in non-human primates and type 2 diabetic subjects. *Cell Metab.* **23**, 427–440 (2016).
- Tillman, E. J. & Rolph, T. FGF21: An emerging therapeutic target for non-alcoholic steatohepatitis and related metabolic diseases. *Front. Endocrinol. (Lausanne)* **11**, 601290–601290 (2020).
- Gaich, G. *et al.* The effects of LY2405319, an FGF21 analog, in obese human subjects with type 2 diabetes. *Cell Metab.* **18**, 333–340 (2013).
- Zarei, M., Pizarro-Delgado, J., Barroso, E., Palomer, X. & Vázquez-Carrera, M. Targeting FGF21 for the treatment of nonalcoholic steatohepatitis. *Trends Pharmacol. Sci.* **41**, 199–208 (2020).
- Lewis, J. E., Ebling, F. J. P., Samms, R. J. & Tsintzas, K. Going back to the biology of FGF21: New insights. *Trends Endocrinol. Metab.* **30**, 491–504 (2019).
- Geng, L., Lam, K. S. L. & Xu, A. The therapeutic potential of FGF21 in metabolic diseases: From bench to clinic. *Nat. Rev. Endocrinol.* **16**, 654–667 (2020).
- Zhen, E. Y., Jin, Z., Ackermann, B. L., Thomas, M. K. & Gutierrez, J. A. Circulating FGF21 proteolytic processing mediated by fibroblast activation protein. *Biochem. J.* **473**, 605–614 (2016).
- Coppage, A. L. *et al.* Human FGF-21 is a substrate of fibroblast activation protein. *PLoS ONE* **11**, e0151269 (2016).
- Sánchez-Garrido, M. A. *et al.* Fibroblast activation protein (FAP) as a novel metabolic target. *Mol. Metab.* **5**, 1015–1024 (2016).
- Dunshie, D. R. *et al.* Fibroblast activation protein cleaves and inactivates fibroblast growth factor 21. *J. Biol. Chem.* **291**, 5986–5996 (2016).
- Fasman, G. D. (ed.) *Circular Dichroism and the Conformational Analysis of Biomolecules* 25–67 (Springer, 1996).
- Greenfield, N. J. Using circular dichroism collected as a function of temperature to determine the thermodynamics of protein unfolding and binding interactions. *Nat. Protoc.* **1**, 2527–2535 (2006).
- Kim, T. D., Ryu, H. J., Cho, H. I., Yang, C.-H. & Kim, J. Thermal behavior of proteins: Heat-resistant proteins and their heat-induced secondary structural changes. *Biochemistry* **39**, 14839–14846 (2000).
- Watanabe, K., Chishiro, K., Kitamura, K. & Suzuki, Y. Proline residues responsible for thermostability occur with high frequency in the loop regions of an extremely thermostable oligo-1,6-glucosidase from *Bacillus thermoglucosidarius* KP1006. *J. Biol. Chem.* **266**, 24287–24294 (1991).
- Remeeva, A. *et al.* Effects of proline substitutions on the thermostable LOV domain from *Chloroflexus aggregans*. *Crystals* **10**, 256 (2020).
- Pignataro, M. F., Herrera, M. G. & Dodero, V. I. Evaluation of peptide/protein self-assembly and aggregation by spectroscopic methods. *Molecules* **25**, 4854 (2020).
- McCoy, J. & La Ville, E. Expression and purification of thioredoxin fusion proteins. *Curr. Protoc. Protein Sci.* **10**, 1–14 (1997).

39. Schenkel, M., Treff, A., Deber, C. M., Krainer, G. & Schlierf, M. Heat treatment of thioredoxin fusions increases the purity of α -helical transmembrane protein constructs. *Protein Sci.* **30**, 1974 (2021).
40. Chen, X., Zaro, J. L. & Shen, W.-C. Fusion protein linkers: Property, design and functionality. *Adv. Drug Deliv. Rev.* **65**, 1357–1369 (2013).
41. Nobbmann, U. *et al.* Dynamic light scattering as a relative tool for assessing the molecular integrity and stability of monoclonal antibodies. *Biotechnol. Genet. Eng. Rev.* **24**, 117–128 (2007).
42. Coskun, T. *et al.* Fibroblast growth factor 21 corrects obesity in mice. *Endocrinology* **149**, 6018–6027 (2008).
43. Xu, J. *et al.* Fibroblast growth factor 21 reverses hepatic steatosis, increases energy expenditure, and improves insulin sensitivity in diet-induced obese mice. *Diabetes* **58**, 250–259 (2009).
44. Yin, J. *et al.* Genetic fusion of human FGF21 to a synthetic polypeptide improves pharmacokinetics and pharmacodynamics in a mouse model of obesity. *Br. J. Pharmacol.* **173**, 2208–2223 (2016).
45. Cui, A. *et al.* The effects of B1344, a novel fibroblast growth factor 21 analog, on nonalcoholic steatohepatitis in nonhuman primates. *Diabetes* **69**, 1611–1623 (2020).
46. Forrey, C., Douglas, J. F. & Gilson, M. K. The fundamental role of flexibility on the strength of molecular binding. *Soft Matter* **8**, 6385–6392 (2012).
47. Chennamsetty, N., Voynov, V., Kayser, V., Helk, B. & Trout, B. L. Design of therapeutic proteins with enhanced stability. *Proc. Natl. Acad. Sci. U.S.A.* **106**, 11937–11942 (2009).
48. Ren, X., Zhao, M., Lash, B., Martino, M. M. & Julier, Z. Growth factor engineering strategies for regenerative medicine applications. *Front. Bioeng. Biotechnol.* **7**, 469 (2020).
49. Kharitonov, A. *et al.* Rational design of a fibroblast growth factor 21-based clinical candidate, LY2405319. *PLoS ONE* **8**, e58575 (2013).
50. Kyte, J. & Doolittle, R. F. A simple method for displaying the hydropathic character of a protein. *J. Mol. Biol.* **157**, 105–132 (1982).
51. Agrawal, A. *et al.* Molecular elements in FGF19 and FGF21 defining KLB/FGFR activity and specificity. *Mol. Metab.* **13**, 45–55 (2018).
52. Paul, S., Sidney, J., Sette, A. & Peters, B. TepiTool: A pipeline for computational prediction of T cell epitope candidates. *Curr. Protoc. Immunol.* **114**, 11–24 (2016).
53. Sette, A. *et al.* The relationship between class I binding affinity and immunogenicity of potential cytotoxic T cell epitopes. *J. Immunol.* **153**, 5586–5592 (1994).
54. Southwood, S. *et al.* Several common HLA-DR types share largely overlapping peptide binding repertoires. *J. Immunol.* **160**(7), 3363–3373 (1998).
55. Wang, P. *et al.* Peptide binding predictions for HLA DR, DP and DQ molecules. *BMC Bioinform.* **11**, 568 (2010).
56. Kolaskar, A. S. & Tongaonkar, P. C. A semi-empirical method for prediction of antigenic determinants on protein antigens. *FEBS Lett.* **276**, 172 (1990).
57. Larsen, J. E. P., Lund, O. & Nielsen, M. Improved method for predicting linear B-cell epitopes. *Immunome Res.* **2**, 2–2 (2006).
58. Jespersen, M. C., Peters, B., Nielsen, M. & Marcatili, P. BepiPred-2.0: Improving sequence-based B-cell epitope prediction using conformational epitopes. *Nucleic Acids Res.* **45**, W24–W29 (2017).

Acknowledgements

This work was supported by the project entitled “Development of Biomedical materials based on marine proteins” (the Ministry of Oceans and Fisheries, Republic of Korea) and the National Research Foundation of Korea (NRF) Grant funded by the Korea government (MSIT) (No. NRF2022R1A5A102641311). CD experiments were supported by Korea Basic Science Institute (National Research Facilities and Equipment Center) Grant funded by the Ministry of Education (2020R 1A 6C 101B194). We thank GENUV Inc. for allowing us to use a Biacore 8K system.

Author contributions

Y.-E.J., K.W.L., and J.H.C. Methodology, Formal analysis, Writing—original draft, review & editing; D.-W.B., B.-G.J., Y.-J.J., Y.J.A., and K.K. Methodology, Writing—original draft; S.-B.P., G.S.L., L.-W.K., and J.H.M. Methodology; J.-H.L., E.-K.K., H.-S.Y., and S.-S.C. Conceptualization, Supervision, Investigation, Funding acquisition, Resources, Methodology, Writing—original draft, review & editing.

Competing interests

The authors declare no competing interests.

Additional information

Supplementary Information The online version contains supplementary material available at <https://doi.org/10.1038/s41598-023-27717-x>.

Correspondence and requests for materials should be addressed to E.-K.K., H.-S.Y. or S.-S.C.

Reprints and permissions information is available at www.nature.com/reprints.

Publisher’s note Springer Nature remains neutral with regard to jurisdictional claims in published maps and institutional affiliations.



Open Access This article is licensed under a Creative Commons Attribution 4.0 International License, which permits use, sharing, adaptation, distribution and reproduction in any medium or format, as long as you give appropriate credit to the original author(s) and the source, provide a link to the Creative Commons licence, and indicate if changes were made. The images or other third party material in this article are included in the article’s Creative Commons licence, unless indicated otherwise in a credit line to the material. If material is not included in the article’s Creative Commons licence and your intended use is not permitted by statutory regulation or exceeds the permitted use, you will need to obtain permission directly from the copyright holder. To view a copy of this licence, visit <http://creativecommons.org/licenses/by/4.0/>.

© The Author(s) 2023